Journal of Quantitative Spectroscopy & Radiative Transfer 111 (2010) 2370–2381

Contents lists available at ScienceDirect

Journal of Quantitative Spectroscopy & Radiative Transfer

journal homepage: www.elsevier.com/locate/jqsrt

Cavity ring-down spectroscopy of the $6\nu_3$ bands of ^{15}N substituted N_2O

K.-F. Song [a], B. Gao [a], A.-W. Liu [a,*], V.I. Perevalov [b], S.A. Tashkun [b], S.-M. Hu [a]

[a] Hefei National Laboratory for Physical Sciences at Microscale, University of Science and Technology of China, Hefei 230026, China
[b] Institute of Atmospheric Optics, Russian Academy of Sciences, Siberian Branch, Tomsk 634055, Russia

ARTICLE INFO

Article history:
Received 9 April 2010
Received in revised form
26 May 2010
Accepted 30 May 2010

Keywords:
Nitrous oxide
Vibration–rotation spectroscopy
Cavity ring-down
Spectroscopic parameters
Effective Hamiltonian

ABSTRACT

The $6\nu_3$ and $\nu_2+6\nu_3-\nu_2$ bands of ^{15}N substituted nitrous oxide isotopologues have been recorded by a continuous-wave cavity ring-down spectrometer (CW-CRDS) operated near 0.8 μm. The sensitivity limit was at the level of 1×10^{-10}/cm. In total, 213, 86 and 191 transitions were observed for the $^{14}N^{15}N^{16}O$, $^{15}N^{14}N^{16}O$ and $^{15}N_2^{16}O$ isotopologues, respectively. The ro-vibrational spectroscopic parameters of the upper states are determined from least square fitting of the transitions. The absolute line intensities of the $6\nu_3$ cold bands have been retrieved by a multi-line fitting procedure from the spectra with an estimated accuracy of 4% for majority of the unblended lines. The vibrational transition dipole moment squared values and the empirical Herman–Wallis coefficients are also presented.

1. Introduction

Nitrous oxide is a minor constituent of the Earth atmosphere. But as a greenhouse gas it plays an important role in the atmospheric radiation balance. It also contributes to the ozone layer depletion. In addition, nitrous oxide is one of the burning products of the organic fuels in the air. As a consequence, the high resolution spectra of this molecule are widely used in various applications like monitoring its concentration in the atmosphere and in the combustion exhaust. The spectra of main isotopologue $^{14}N_2^{16}O$ nitrous oxide has been systematically studied up to 669 nm [1]. And in the last few decades, spectroscopic studies of single ^{15}N substituted nitrous oxide ($^{14}N^{15}N^{16}O$ and $^{15}N^{14}N^{16}O$) have been carried out with microwave spectrometers (MW) [2–4], Fourier-transform infrared (FT-IR) spectrometers (FTS) [5–11], intra-cavity laser absorption spectrometer (ICLAS) [12], and cavity ring-down spectrometer (CRDS) [13–15]. All the above listed measurements were carried out with natural nitrous oxide samples where the abundance of the single ^{15}N substituted isotopologue is 0.36409% given in Hitran database. Using ^{15}N enriched samples, the FT-IR spectroscopy above 1 μm of $^{14}N^{15}N^{16}O$, $^{15}N^{14}N^{16}O$ and $^{15}N_2^{16}O$ has been reported in Refs. [16–19,21].

Here we present the cavity ring-down spectroscopy of these three ^{15}N substituted nitrous oxide isotopologues near the 0.8 μm region where the $6\nu_3$ overtone bands are located. Since only the spectral data over 1 μm have been employed in the recently developed global effective Hamiltonian (EH) calculations of these molecules [20,21], the new spectral data below 1 μm presented here can be an interesting example to check the extrapolation and prediction capability of the EH models.

The present paper is organized as following: In Section 2, the experimental procedure and the methodology of the analysis are presented. Section 3 is devoted to the band by band analysis and the modeling of the spectral parameters. Conclusions are given in the last section. Note that throughout the paper we use the notation for the isotopologues according to HITRAN [22]: $^{14}N^{15}N^{16}O$: 456, $^{15}N^{14}N^{16}O$: 546, and $^{15}N_2^{16}O$: 556.

* Corresponding author. Tel./fax: +86 551 3607632.
E-mail address: awliu@ustc.edu.cn (A.-W. Liu).

0022-4073/$ - see front matter © 2010 Elsevier Ltd. All rights reserved.
doi:10.1016/j.jqsrt.2010.05.022

2. Experiment and data reduction

The CW-CRDS spectrometer has been developed using a CW tunable Ti-sapphire laser over the spectral range of 780–830 nm. The details of the cavity ring-down spectrometer are presented in Refs. [23,24]. In brief, the structure of the setup is as following: A CW tunable Ti:sapphire laser (Coherent 899-21) beam is carefully coupled into a 1.2 m long resonance cavity. The cavity mirrors (Los Gatos Inc.) have a reflectivity of 99.995% and one of the two mirrors is mounted on a piezoelectric actuator (PI Inc.). The piezoelectric actuator is driven with a triangle wave from a function generator. The Ti:Sa laser is running in a step-scan mode controlled by a personal computer (PC). On each step, typically about 100 ring-down events are recorded with a fast digitizer (ADLINK PCI-9820). The digitizer is working at a sampling rate of 1 MS/s (Mega-samples per second) with 14-bit resolution. A fitting program which follows the method proposed by Halmer et al. [25] is applied to fit the exponentially decay curve and to give the decay time τ. The sample absorption coefficient, α, can be derived from

$$\alpha = \frac{1}{c}\left(\frac{1}{\tau} - \frac{1}{\tau_0}\right), \tag{1}$$

where c is the speed of light, τ and τ_0 are the decay time of the cavity with and without sample, respectively. The minimum detectable absorption coefficient of the present spectrometer has been demonstrated to be 7×10^{-11}/cm [24].

Three samples with 456, 546 or 556 enriched nitrous oxide isotopes were purchased from Icon Services Inc. The stated isotopic concentrations of 456, 546 and 556 are all 99% in respective samples. Photo-ionization mass spectroscopy (PIMS) combined with IR spectroscopy gave the abundances of 97.4%, 97.6% and 97.6% (with about 0.2% uncertainty) for N_2O-456, 546 or 556 in respective samples. PIMS was performed with a time-of-flight mass spectrometer in the photochemistry end-station in National Synchrotron Radiation Laboratory (NSRL), Hefei.

Table 1
Experimental conditions applied in the ^{15}N enriched nitrous oxide spectra measurements.

Sample	Isotope abundance (%)	Pressure (Torr)	Temperature (K)	Spectral region (cm^{-1})
N_2O-456	97.4	59.7	297.2 ±1.0	12 508–12 646
N_2O-546	97.6	23.0	297.8 ±1.0	12600–12 766
N_2O-556	97.6	52.8	297.4 ±1.0	12402–12 560

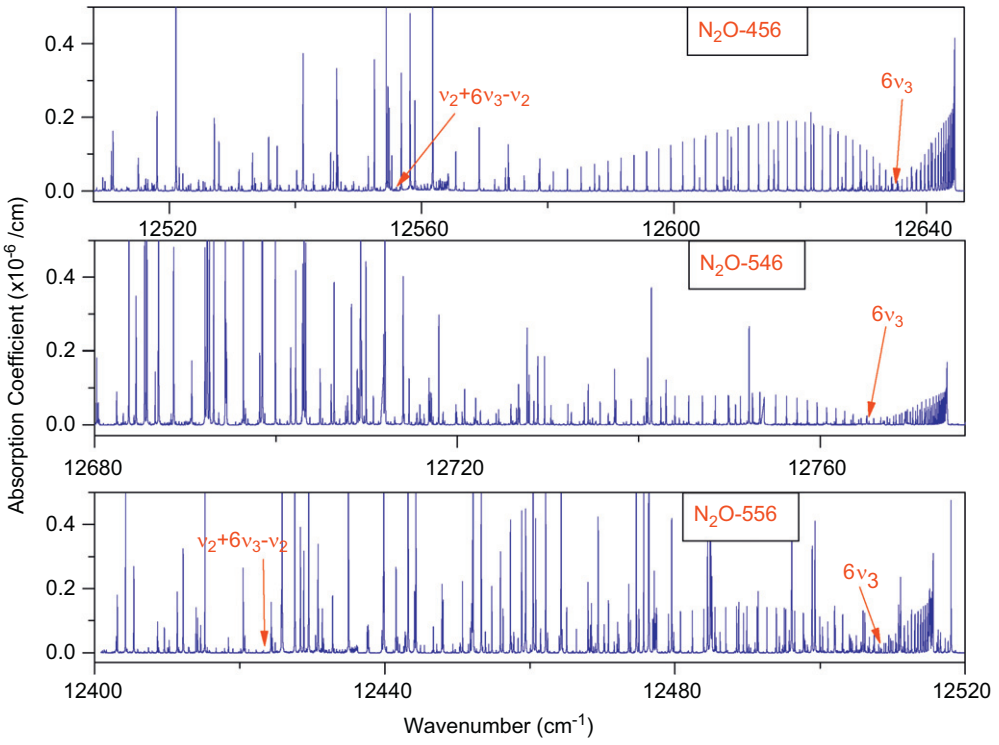

Fig. 1. Overview of the CW-CRDS spectrum of three ^{15}N substituted nitrous oxide samples around the $6\nu_3$ band region. Upper panel: N_2O-456 enriched sample, 59.7 Torr. Middle panel: N_2O-546 enriched sample, 23.0 Torr. Lower panel: N_2O-556 enriched sample, 52.8 Torr.

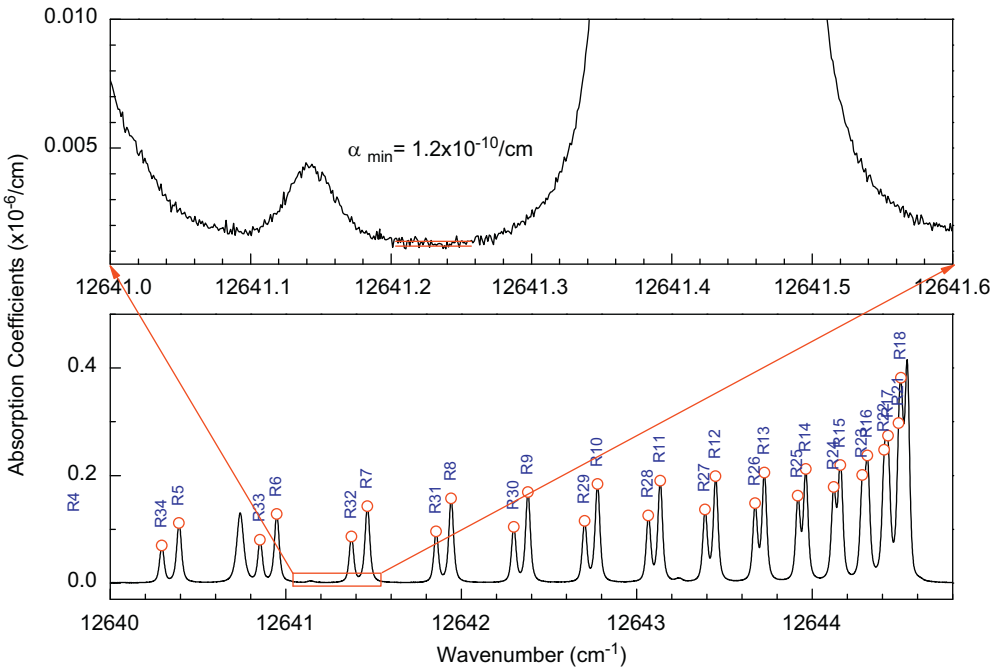

Fig. 2. The R-branch of the $6\nu_3$ band of $^{14}N^{15}N^{16}O$ around 12 642.5 cm^{-1}. The rotational assignments are presented. The enlargement illustrates the achieved minimum detectable absorption loss $\alpha_{min} = 1.2 \times 10^{-10}$/cm.

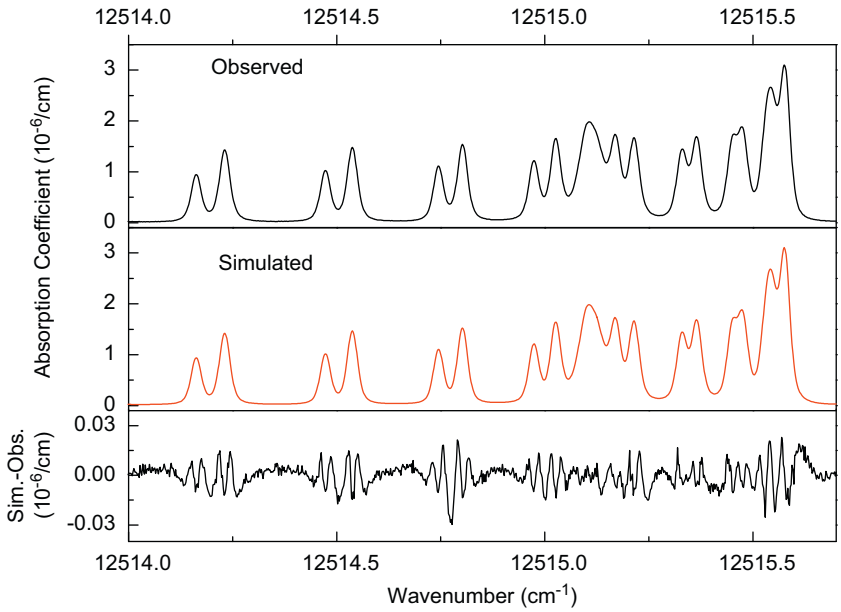

Fig. 3. Comparison of the experimental CRDS spectrum of $^{15}N_2^{16}O$ and the simulated spectrum obtained from the multi-line fitting. The residuals are displayed on the lower panel.

The gas sample pressure was measured using capacitance manometers (MKS Baratron 627B) with accuracy of 0.15%. The experimental conditions are presented in Table 1.

The calibration of the spectrum is based on the readings given by a λ−meter (Burleigh WA1500). The water line positions from the Hitran 2008 database [22] were used as absolute reference wavenumbers. An overview of the CW-CRDS spectra is presented in Fig. 1. A small part of the N_2O-456 spectrum is presented in Fig. 2 which illustrates the R branch of $6\nu_3$ band

$^{14}N^{15}N^{16}O$. The signal to noise ratio analysis shows the noise equivalent minimum detectable absorption loss is about 1.2×10^{-10}/cm.

3. Results

3.1. Transition list

The $6\nu_3$ cold bands of each of the ^{15}N substituted nitrous oxide isotopologues and the $\nu_2+6\nu_3-\nu_2$ hot bands for 456 and 556 isotopologues were observed for the first time. The line parameters of each observed line were retrieved by using an interactive least squares multi-lines fitting procedure. Since the instrumental linewidth which was estimated as $<1\times10^{-4}\,cm^{-1}$ [24] is much smaller than the Doppler broadening, the instrumental profile was neglected in the fitting. A Voigt line profile was adopted and the Gaussian component was fixed to the calculated Doppler broadening profile. Line position, integrated line absorbance, Lorentzian width of each line and a baseline were obtained by the fitting procedure ("Intwin" [11]). Fig. 3 illustrates a piece of the experimental spectrum and the simulated spectrum obtained from the fitting. Altogether 94, 86 and 95 lines have been observed for the $6\nu_3$ cold band of 456, 546 and 556 isotopologues, respectively. The uncertainties of the unblended and not-very-weak lines are estimated to be $0.001\,cm^{-1}$ for the line positions. The main error on the line strength values comes from the line profile fitting, especially the uncertainty on the baseline. The fitting residual between the experimental spectrum and the simulated spectrum is estimated to be around 3.5% for well-isolated and unblended lines. We estimate that such fitting residual can contribute about 1–2% error to the resulted line intensity values. Including the pressure uncertainty (0.15%) and the error from the temperature fluctuation ($<1\%$), the accuracy of the line intensities should be better than 4% for majority of the lines. For those blended lines, the error may reach 10% since the baseline uncertainty is supposed to be much larger.

The obtained line position and strength values are presented in Tables 3–5 to the $6\nu_3$ cold bands. The line strength values in the tables are given for a pure isotopologue abundance at 296 K.

3.2. Spectroscopic constants of the upper states

The rotational analysis was carried out using the combination difference method, using literature constants for the ground and $(0\,1^1\,0)$ states [6,26]. The standard expression below for the vibration–rotation energy levels was used to determine the spectroscopic parameters:

$$F_v(J) = G_v + B_v J(J+1) - D_v J^2(J+1)^2 + H_v J^3(J+1)^3. \quad (2)$$

In Eq. (2), G_v is the vibrational term value, B_v is the rotational constant, D_v and H_v are the centrifugal distortion constants. The spectroscopic parameters for an upper state were fitted directly to the observed line positions of the respective band, and in the case of hot bands involving *e* and *f* rotational levels, the *ee*, and *ff* sub bands were considered independently. The lower state rotational constants were constrained to their literature values [26] in the fitting. The observed line positions together with the residuals are given in the Supplementary Material of this paper. The spectroscopic parameters retrieved from the fitting are presented in Table 2.

From the fitting results, we can easily identify the perturbations to the energy levels of the upper states. The upper panels of Figs. 4–6 show the deviation between

Table 2
Ro-vibrational parameters of the observed bands of $^{14}N^{15}N^{16}O$, $^{15}N^{14}N^{16}O$ and $^{15}N_2^{16}O$, in cm^{-1}.

ISO	State[a]	G_V[b]	B_V	$D_V\times10^7$	$H_V\times10^{11}$	n/N[c]	RMS $\times10^3$
456	0000e	0.00000	0.418981810	1.763264			
456	0110e	575.43365	0.419108916	1.785826			
456	0110f	575.43365	0.419918641	1.794459			
456	0006e	12 636.20574(23)	0.3989425(19)	1.901(36)	3.10(18)	73/94	0.86
456	0116e	13 131.11502(78)	0.3994889(66)	0.75(72)		22/60	1.61
456	0116f	13 131.1262(11)	0.4001812(78)	−1.68(11)		22/59	2.29
546	0000e	0.00000	0.404857965	1.642938	0.018666		
546	0006e	12 766.19628(35)	0.3849472(24)	2.656(37)	6.94(16)	60/86	1.10
556	0000e	0.00000	0.404860200	1.635600			
556	0110e	571.89400	0.405002100	1.656000			
556	0110f	571.89400	0.405761700	1.663800			
556	0006e	12 507.54850(30)	0.3853993(21)	0.601(26)		43/95	0.97
556	0116e	12 999.59591(81)	0.3862890(61)	−1.523(84)		32/41	2.00
556	0116f	12 999.60841(95)	0.3869657(68)	−7.299(97)		27/42	2.04

Note: The lower state constants were fixed at the values of Refs. [6,26]. The uncertainties are given in parenthesis in the unit of the last quoted digit.
[a] Normal mode labeling $v_1v_2\ell_2v_3\Gamma$.
[b] The upper vibrational term value.
[c] n: number of transitions included in the fit; N: number of assigned rotational transitions.

Table 3
Observed transitions of the $6\nu_3$ band of $^{14}N^{15}N^{16}O$.

Line	Position	S_{obs}	S_{cal}	%	$\|R\|^2_{obs.}$
P45†	12 559.53205	1.26E−28	3.06E−28	143	1.21E−10
P44†	12 561.86725	2.45E−28	3.58E−28	46	2.00E−10
P42†	12 566.72565	5.60E−28	4.82E−28	−14	3.36E−10
P40†	12 571.56775	6.50E−28	6.38E−28	−1.9	2.93E−10
P39†	12 573.94515	7.12E−28	7.29E−28	2.3	2.79E−10
P38	12 576.28775	8.30E−28	8.29E−28	−0.2	2.85E−10
P37	12 578.59465	9.81E−28	9.38E−28	−4.4	2.96E−10
P36	12 580.86285	1.06E−27	1.06E−27	−0.2	2.83E−10
P35	12 583.09205	1.24E−27	1.18E−27	−4.6	2.95E−10
P34	12 585.28475	1.29E−27	1.32E−27	2.4	2.73E−10
P33	12 587.43985	1.46E−27	1.47E−27	0.7	2.77E−10
P32	12 589.55235	1.67E−27	1.62E−27	−3.0	2.86E−10
P31	12 591.62750	1.79E−27	1.78E−27	−0.5	2.78E−10
P30	12 593.66268	1.91E−27	1.95E−27	2.4	2.69E−10
P29	12 595.65853	2.13E−27	2.12E−27	−0.4	2.76E−10
P28	12 597.61595	2.26E−27	2.30E−27	1.9	2.69E−10
P27	12 599.53172	2.46E−27	2.48E−27	0.9	2.71E−10
P26	12 601.40860	2.64E−27	2.66E−27	0.6	2.71E−10
P25	12 603.24677	2.90E−27	2.83E−27	−2.4	2.78E−10
P24	12 605.04581	3.04E−27	3.00E−27	−1.4	2.74E−10
P23	12 606.80233	3.22E−27	3.16E−27	−1.7	2.75E−10
P22	12 608.52088	3.39E−27	3.31E−27	−2.3	2.76E−10
P21	12 610.19825	3.44E−27	3.45E−27	0.4	2.67E−10
P20	12 611.83825	3.56E−27	3.57E−27	0.4	2.67E−10
P19	12 613.43665	3.66E−27	3.67E−27	0.4	2.66E−10
P18	12 614.99365	3.85E−27	3.75E−27	−2.5	2.74E−10
P17	12 616.51215	3.91E−27	3.81E−27	−2.6	2.73E−10
P16	12 617.99195	3.86E−27	3.83E−27	−0.7	2.67E−10
P15	12 619.43045	3.92E−27	3.83E−27	−2.5	2.72E−10
P14	12 620.82915	3.80E−27	3.79E−27	−0.1	2.65E−10
P13	12 622.18785	3.73E−27	3.72E−27	−0.1	2.64E−10
P12	12 623.50655	3.69E−27	3.62E−27	−2.0	2.69E−10
R52†	12624.66495	8.67E−29	9.40E−29	8.5	2.83E−10
P11	12 624.78585	3.41E−27	3.48E−27	2.1	2.58E−10
R51†	12 625.84891	9.76E−29	1.13E−28	16	2.63E−10
P10	12 626.02375	3.25E−27	3.30E−27	1.4	2.59E−10
R50†	12 627.00495	1.09E−28	1.36E−28	25	2.43E−10
P9	12 627.22235	3.11E−27	3.09E−27	−0.7	2.64E−10
R49†	12 628.12936	1.92E−28	1.62E−28	−15	3.56E−10
P8	12 628.38105	2.82E−27	2.85E−27	1.0	2.60E−10
R48†	12 629.21185	1.78E−28	1.93E−28	8.4	2.77E−10
P7	12 629.50065	2.64E−27	2.57E−27	−2.4	2.69E−10
R47†	12 630.25205	2.76E−28	2.29E−28	−17	3.60E−10
P6	12 630.57685	2.39E−27	2.27E−27	−5.2	2.76E−10
R46†	12 631.23365	2.44E−28	2.70E−28	11	2.69E−10
P5	12 631.61555	1.95E−27	1.94E−27	−0.9	2.64E−10
R45†	12 632.14305	2.54E−28	3.17E−28	25	2.37E−10
P4	12 632.61345	1.60E−27	1.58E−27	−1.6	2.66E−10
R44†	12 632.92565	2.67E−28	3.70E−28	39	2.12E−10
P3	12 633.57205	1.23E−27	1.20E−27	−2.5	2.68E−10
R43†	12 633.99085	2.66E−28	4.31E−28	62	1.81E−10
P2	12 634.49085	8.26E−28	8.12E−28	−1.7	2.66E−10
R42†	12 634.65445	3.75E−28	4.99E−28	33	2.19E−10
R41†	12 635.36905	4.48E−28	5.75E−28	29	2.26E−10
P1	12 635.36905	4.48E−28	4.09E−28	−8.6	2.86E−10
R40†	12 636.17585	5.86E−28	6.60E−28	13	2.56E−10
R39†	12 636.94045	6.96E−28	7.55E−28	8.4	2.65E−10
R0	12 637.00375	3.72E−28	4.11E−28	11	2.37E−10
R38†	12 637.67875	1.13E−27	8.58E−28	−24	3.77E−10
R1	12 637.76255	7.97E−28	8.19E−28	2.7	2.55E−10
R37†	12 638.38745	9.47E−28	9.72E−28	2.7	2.77E−10
R2	12 638.48045	1.17E−27	1.22E−27	4.6	2.50E−10
R36	12 639.06015	1.06E−27	1.10E−27	3.0	2.75E−10
R3	12 639.15795	1.54E−27	1.61E−27	4.2	2.51E−10
R35	12 639.69655	1.33E−27	1.23E−27	−7.8	3.06E−10
R4	12 639.79605	1.94E−27	1.98E−27	2.1	2.56E−10
R34	12 640.29405	1.35E−27	1.37E−27	1.8	2.76E−10
R5	12 640.39215	2.26E−27	2.33E−27	3.0	2.54E−10
R33	12 640.85395	1.54E−27	1.52E−27	−0.9	2.82E−10

Table 3 (*continued*)

Line	Position	S_{obs}	S_{cal}	%	$\|R\|^2_{obs.}$
R6	12 640.94895	2.58E−27	2.65E−27	2.5	2.56E−10
R32	12 641.37435	1.66E−27	1.69E−27	1.7	2.74E−10
R7	12 641.46535	2.87E−27	2.95E−27	2.5	2.56E−10
R31	12 641.85685	1.84E−27	1.86E−27	0.9	2.75E−10
R8	12 641.94255	3.13E−27	3.21E−27	2.5	2.56E−10
R30	12 642.29955	2.02E−27	2.03E−27	0.6	2.75E−10
R9	12 642.38015	3.38E−27	3.44E−27	1.9	2.58E−10
R29	12 642.70305	2.21E−27	2.21E−27	0.0	2.76E−10
R10	12 642.77635	3.67E−27	3.64E−27	−0.9	2.66E−10
R28	12 643.06685	2.40E−27	2.40E−27	−0.1	2.75E−10
R11	12 643.13365	3.75E−27	3.80E−27	1.6	2.60E−10
R27	12 643.38955	2.61E−27	2.59E−27	−0.8	2.76E−10
R12	12 643.44985	3.89E−27	3.93E−27	1.0	2.62E−10
R26	12 643.67445	2.81E−27	2.78E−27	−1.3	2.77E−10
R13	12 643.72705	4.00E−27	4.02E−27	0.6	2.63E−10
R25	12 643.91845	2.98E−27	2.96E−27	−0.6	2.74E−10
R14	12 643.96305	4.03E−27	4.08E−27	1.1	2.62E−10
R24	12 644.12235	3.28E−27	3.14E−27	−4.2	2.83E−10
R15	12 644.16075	4.27E−27	4.10E−27	−4.1	2.77E−10
R23	12 644.28595	3.39E−27	3.32E−27	−2.1	2.76E−10
R16	12 644.31505	4.07E−27	4.09E−27	0.5	2.65E−10
R22	12 644.41025	3.65E−27	3.48E−27	−4.5	2.83E−10
R17	12 644.43175	4.08E−27	4.05E−27	−0.8	2.69E−10
R21*	12 644.49215	2.64E−27	3.63E−27	38	1.95E−10
R18*	12 644.50605	5.37E−27	3.98E−27	−26	3.60E−10

† Perturbed transitions.
* Blended lines.

Table 4
Observed transitions of the $6v_3$ band of $^{15}N^{14}N^{16}O$.

Line	Position	S_{obs}	S_{cal}	%	$\|R\|^2_{obs.}$
P46†	12 688.03886	1.76E−28	2.61E−28	48	1.75E−10
P45†	12 690.57310	6.86E−28	3.05E−28	−56	5.82E−10
P43†	12 695.55462	3.77E−28	4.13E−28	9.5	2.36E−10
P42†	12 698.00734	4.88E−28	4.77E−28	−2.2	2.64E−10
P41	12 700.42277	5.50E−28	5.49E−28	−0.3	2.59E−10
P40	12 702.80645	7.56E−28	6.28E−28	−17	3.10E−10
P39	12 705.15081	7.76E−28	7.16E−28	−7.7	2.78E−10
P37	12 709.73269	8.74E−28	9.17E−28	4.9	2.44E−10
P35	12 714.16398	1.61E−27	1.15E−27	−28	3.57E−10
P34	12 716.32201	1.25E−27	1.29E−27	3.1	2.48E−10
P33	12 718.44326	1.30E−27	1.42E−27	9.4	2.33E−10
P32	12 720.52413	1.58E−27	1.57E−27	−0.6	2.57E−10
P31	12 722.56570	1.79E−27	1.72E−27	−3.4	2.64E−10
P30	12 724.56972	1.84E−27	1.88E−27	2.6	2.48E−10
P29	12 726.53257	1.99E−27	2.05E−27	3.1	2.47E−10
P28	12 728.45729	2.17E−27	2.21E−27	1.8	2.49E−10
P27	12 730.34223	2.39E−27	2.38E−27	−0.5	2.55E−10
P26	12 732.18867	2.52E−27	2.55E−27	1.1	2.51E−10
P25	12 733.99488	2.75E−27	2.71E−27	−1.5	2.57E−10
P24*	12 735.76085	2.83E−27	2.87E−27	1.4	2.50E−10
P23	12 737.48782	2.96E−27	3.02E−27	2.2	2.47E−10
P22	12 739.17560	3.12E−27	3.16E−27	1.5	2.49E−10
P21	12 740.82267	3.09E−27	3.29E−27	6.3	2.37E−10
P20	12 742.43247	3.42E−27	3.40E−27	−0.7	2.54E−10
P19	12 743.99943	3.53E−27	3.49E−27	−1.0	2.55E−10
P18*	12 745.52737	3.69E−27	3.56E−27	−3.4	2.61E−10
P17	12 747.01191	3.61E−27	3.61E−27	0.1	2.52E−10
P16	12 748.45985	3.65E−27	3.63E−27	−0.4	2.53E−10
P15†	12 749.87050	3.94E−27	3.62E−27	−8.1	2.74E−10
P14	12 751.23451	3.94E−27	3.59E−27	−8.9	2.76E−10
P13	12 752.56322	3.41E−27	3.52E−27	3.3	2.43E−10

Table 4 (*continued*)

Line	Position	S_{obs}	S_{cal}	%	$\|R\|^2_{obs.}$
P12	12 753.85072	3.45E−27	3.42E−27	−1.0	2.54E−10
P11*	12 755.09659	3.21E−27	3.28E−27	2.4	2.45E−10
P10*	12 756.30327	3.04E−27	3.12E−27	2.4	2.45E−10
P9*	12 757.47142	2.86E−27	2.92E−27	1.8	2.46E−10
P8*	12 758.60031	2.68E−27	2.68E−27	0.4	2.50E−10
P7	12 759.69364	2.40E−27	2.42E−27	1.1	2.48E−10
R45†	12 760.66400	2.40E−28	3.14E−28	31.1	1.98E−10
P6	12 760.73981	2.10E−27	2.14E−27	1.6	2.47E−10
R44†	12 761.59861	2.84E−28	3.67E−28	29	2.01E−10
P5*	12 761.74778	1.79E−27	1.82E−27	1.6	2.47E−10
R43†	12 762.51542	4.73E−28	4.26E−28	−10	2.88E−10
P4*	12 762.71551	1.52E−27	1.49E−27	−2.0	2.56E−10
R42†	12 763.41143	4.54E−28	4.92E−28	8.2	2.39E−10
P3*	12 763.64435	1.21E−27	1.13E−27	−6.4	2.68E−10
R41†	12 764.28042	5.17E−28	5.66E−28	9.4	2.36E−10
P2	12 764.53716	7.49E−28	7.64E−28	2.0	2.46E−10
R40†	12 765.11942	6.29E−28	6.48E−28	3.0	2.50E−10
P1	12 765.38645	3.84E−28	3.85E−28	0.3	2.50E−10
R39	12 765.92372	7.22E−28	7.39E−28	2.3	2.52E−10
R38	12 766.69142	8.01E−28	8.39E−28	4.7	2.46E−10
R0	12 766.96591	4.44E−28	3.87E−28	−13	2.88E−10
R37	12 767.42390	9.37E−28	9.48E−28	1.2	2.54E−10
R1	12 767.69571	8.01E−28	7.70E−28	−3.9	2.61E−10
R36	12 768.12028	1.03E−27	1.07E−27	3.9	2.47E−10
R2	12 768.38682	1.34E−27	1.15E−27	−15	2.93E−10
R35	12 768.77935	1.28E−27	1.19E−27	−6.6	2.74E−10
R3	12 769.03835	1.53E−27	1.51E−27	−1.0	2.53E−10
R34	12 769.39967	1.37E−27	1.33E−27	−2.6	2.63E−10
R4	12 769.64669	1.88E−27	1.86E−27	−1.2	2.54E−10
R33	12 769.98051	1.42E−27	1.48E−27	4.1	2.45E−10
R5*	12 770.22081	2.15E−27	2.19E−27	1.9	2.46E−10
R32*	12 770.52602	1.66E−27	1.63E−27	−2.1	2.61E−10
R6*	12 770.75097	2.54E−27	2.49E−27	−1.8	2.55E−10
R31	12 771.03038	1.85E−27	1.79E−27	−3.1	2.63E−10
R7	12 771.24107	2.78E−27	2.77E−27	−0.2	2.51E−10
R30*	12 771.49733	1.88E−27	1.96E−27	4.1	2.45E−10
R8	12 771.69200	2.93E−27	3.02E−27	3.3	2.43E−10
R29	12 771.92307	2.13E−27	2.13E−27	−0.3	2.55E−10
R9	12 772.10371	3.21E−27	3.24E−27	1.2	2.48E−10
R10	12 772.47387	3.35E−27	3.43E−27	2.4	2.45E−10
R27†	12 772.65933	2.71E−27	2.48E−27	−8.6	2.78E−10
R11	12 772.80561	3.51E−27	3.59E−27	2.1	2.46E−10
R26	12 772.96642	2.58E−27	2.66E−27	2.8	2.47E−10
R12	12 773.09695	3.67E−27	3.71E−27	1.0	2.49E−10
R25	12 773.23576	2.78E−27	2.83E−27	1.7	2.49E−10
R13	12 773.34693	3.84E−27	3.80E−27	−1.1	2.54E−10
R24	12 773.46425	2.94E−27	3.00E−27	2.0	2.48E−10
R14	12 773.55785	3.79E−27	3.85E−27	1.8	2.47E−10
R23	12 773.65359	3.07E−27	3.16E−27	3.2	2.45E−10
R15	12 773.72831	3.80E−27	3.88E−27	2.0	2.47E−10
R22	12 773.80240	3.19E−27	3.32E−27	3.8	2.44E−10
R16	12 773.85916	3.96E−27	3.87E−27	−2.2	2.57E−10
R21	12 773.91099	3.96E−27	3.46E−27	−13	2.89E−10
R17	12 773.94972	4.32E−27	3.83E−27	−11	2.84E−10
R18*	12 774.00496	8.66E−27	3.77E−27	−56	5.79E−10

† Perturbed transitions.
* Blended lines.

the observed position and the one calculated from the parameters of $(00^{0}6)$ vibrational states in Table 2 without considering the perturbations. The perturbations of the $(00^{0}6)$ state start from $J=40$, 37 and 30 for the 456, 546 and 556 isotopologues, respectively.

The global fitting of the observed transitions (below 9000 cm^{-1} so far) has been presented by Tashkun et al. [20] (for N_2O 456 and 546) and by Lyulin et al. [21] (for N_2O 556) using the effective Hamiltonian (EH) approach. It is interesting to compare the line positions newly observed here and those predicted using extrapolating the EH calculations. The (*obs.–pred.*) deviations of the line positions of the $(00^{0}6)$ states of three isotopologues are shown on the lower panels of Figs. 4–6. Apparently, due to the lack of input experimental information above 9000 cm^{-1}, the predictive ability of the EH models for

Table 5
Observed transitions of the $6v_3$ band of $^{15}N_2^{16}O$.

Line	Position	S_{obs}	S_{cal}	%	$\|R\|^2_{obs.}$
P52†	12 415.47372	8.63E−30	5.90E−29	584	1.66E−11
P51†	12 418.11794	3.11E−29	7.19E−29	131	4.98E−11
P50†	12 420.61295	4.29E−29	8.72E−29	103	5.73E−11
P49†	12 423.10819	1.01E−28	1.05E−28	4.6	1.13E−10
P48†	12 425.59989	8.17E−29	1.27E−28	55	7.70E−11
P47†	12 428.10492	1.36E−28	1.51E−28	11	1.09E−10
P46†	12 430.57156	2.58E−28	1.80E−28	−30	1.75E−10
P45†	12 433.03186	2.48E−28	2.14E−28	−14	1.43E−10
P44†	12 435.46356	3.31E−28	2.52E−28	−24	1.64E−10
P43†	12 437.87904	3.08E−28	2.96E−28	−3.8	1.31E−10
P42†	12 440.25699	3.55E−28	3.46E−28	−2.6	1.31E−10
P41†	12 442.60473	4.02E−28	4.02E−28	−0.1	1.29E−10
P40†	12 444.91325	4.76E−28	4.65E−28	−2.2	1.33E−10
P39†	12 447.17790	5.69E−28	5.36E−28	−5.9	1.39E−10
P38†	12 449.38222	6.01E−28	6.14E−28	2.1	1.29E−10
P37†	12 451.49960	5.32E−28	7.00E−28	32	1.01E−10
P36†	12 454.32335	6.14E−28	7.95E−28	29	1.04E−10
P35†	12 456.35685	8.33E−28	8.98E−28	7.8	1.26E−10
P34†	12 458.40705	9.77E−28	1.01E−27	3.3	1.32E−10
P32†	12 462.47600	1.30E−27	1.26E−27	−3.7	1.44E−10
P31†	12 464.46703	1.40E−27	1.39E−27	−0.7	1.41E−10
P30*	12 466.42508	1.58E−27	1.53E−27	−3.1	1.45E−10
P29	12 468.34872	1.80E−27	1.68E−27	−6.8	1.52E−10
P28*	12 470.23475	1.85E−27	1.83E−27	−1.5	1.45E−10
P27*	12 472.08620	2.04E−27	1.98E−27	−3.3	1.48E−10
P26	12 473.90023	2.13E−27	2.13E−27	−0.2	1.45E−10
P24	12 477.41334	2.47E−27	2.43E−27	−1.6	1.48E−10
P23	12 479.11242	2.58E−27	2.58E−27	−0.3	1.47E−10
P22	12 480.77223	2.81E−27	2.71E−27	−3.3	1.53E−10
P21	12 482.39624	2.84E−27	2.84E−27	−0.1	1.48E−10
P20	12 483.98087	2.96E−27	2.95E−27	−0.2	1.49E−10
P19	12 485.52501	3.02E−27	3.05E−27	1.0	1.48E−10
P18	12 487.03141	3.10E−27	3.12E−27	0.9	1.49E−10
P17	12 488.49974	3.15E−27	3.18E−27	1.0	1.49E−10
P16	12 489.93165	3.18E−27	3.21E−27	1.1	1.50E−10
P15	12 491.32302	3.16E−27	3.22E−27	2.0	1.49E−10
P14	12 492.67619	3.10E−27	3.20E−27	3.3	1.48E−10
P13	12 493.98980	3.12E−27	3.15E−27	1.1	1.51E−10
P12	12 495.26555	3.05E−27	3.07E−27	0.8	1.52E−10
P11*	12 496.50701	2.94E−27	2.96E−27	0.6	1.53E−10
P10	12 497.69960	2.83E−27	2.82E−27	−0.3	1.55E−10
P9	12 498.86112	2.80E−27	2.64E−27	−5.7	1.64E−10
R49†	12 499.72728	6.55E−29	1.42E−28	117	7.15E−11
P8	12 499.98167	2.63E−27	2.44E−27	−7.0	1.67E−10
R48†	12 500.61443	7.78E−29	1.70E−28	118	7.14E−11
P7	12 501.06325	2.25E−27	2.22E−27	−1.2	1.58E−10
R47†	12 501.50005	1.23E−28	2.02E−28	64	9.54E−11
P6	12 502.10483	1.94E−27	1.96E−27	0.9	1.55E−10
R46†	12 502.38536	1.38E−28	2.38E−28	72	9.12E−11
R45†	12 503.27165	1.76E−28	2.79E−28	59	9.88E−11
P4	12 504.07414	1.34E−27	1.37E−27	2.2	1.53E−10
R44†	12 504.13066	2.63E−28	3.26E−28	24	1.27E−10
P3*	12 505.00161	1.22E−27	1.04E−27	−15	1.84E−10
R42†	12 505.80115	3.76E−28	4.38E−28	17	1.35E−10
R41†	12 506.60194	4.20E−28	5.04E−28	20	1.30E−10
P1*	12 506.74229	3.56E−28	3.53E−28	−0.7	1.58E−10
R40†	12 507.36964	4.86E−28	5.77E−28	19	1.32E−10
R39†	12 508.10303	5.45E−28	6.58E−28	21	1.29E−10
R0	12 508.32009	3.67E−28	3.53E−28	−3.8	1.62E−10
R38†	12 508.79868	6.19E−28	7.45E−28	20	1.29E−10
R1	12 509.05096	7.56E−28	7.01E−28	−7.3	1.67E−10
R37†	12 509.44567	4.15E−28	8.40E−28	103	7.64E−11
R2	12 509.74489	1.04E−27	1.04E−27	0.2	1.54E−10
R36†	12 510.04254	8.17E−28	9.41E−28	15	1.34E−10
R3	12 510.39812	1.41E−27	1.36E−27	−3.3	1.59E−10
R35†	12 510.54550	6.51E−28	1.05E−27	61	9.50E−11
R4	12 511.01390	1.75E−27	1.66E−27	−5.0	1.61E−10
R5	12 511.58914	1.99E−27	1.94E−27	−2.3	1.55E−10
R34†	12 511.75258	7.16E−28	1.15E−27	61	9.37E−11

Table 5 (*continued*)

Line	Position	S_{obs}	S_{cal}	%	$\|R\|^2_{obs.}$
R6	12 512.12699	2.25E−27	2.20E−27	−2.3	1.54E−10
R33†	12 512.16899	1.00E−27	1.27E−27	27	1.18E−10
R7	12 512.62639	2.52E−27	2.42E−27	−3.9	1.55E−10
R31†	12 513.03996	1.43E−27	1.53E−27	6.9	1.39E−10
R8	12 513.08664	2.72E−27	2.62E−27	−3.9	1.54E−10
R30†	12 513.44444	1.90E−27	1.66E−27	−13	1.68E−10
R9	12 513.50586	2.94E−27	2.78E−27	−5.5	1.55E−10
R29†	12 513.82070	1.80E−27	1.79E−27	−0.6	1.46E−10
R10	12 513.88671	3.06E−27	2.90E−27	−5.2	1.52E−10
R28	12 514.16235	1.99E−27	1.91E−27	−3.8	1.49E−10
R11	12 514.23093	3.29E−27	2.98E−27	−9.5	1.57E−10
R27	12 514.47275	2.15E−27	2.02E−27	−5.9	1.50E−10
R12	12 514.53756	3.30E−27	3.03E−27	−8.1	1.52E−10
R26	12 514.74436	2.29E−27	2.14E−27	−6.6	1.49E−10
R13	12 514.80228	3.39E−27	3.06E−27	−9.8	1.53E−10
R25*	12 514.97357	2.53E−27	2.25E−27	−11	1.54E−10
R14	12 515.02610	3.58E−27	3.05E−27	−15	1.59E−10
R24*	12 515.16994	2.97E−27	2.34E−27	−21	1.71E−10
R15	12 515.21453	3.42E−27	3.02E−27	−12	1.51E−10
R23*	12 515.32918	2.78E−27	2.43E−27	−13	1.51E−10
R16	12 515.36499	3.41E−27	2.93E−27	−14	1.51E−10
R22*	12 515.44987	2.87E−27	2.48E−27	−14	1.49E−10
R17	12 515.47565	3.38E−27	2.85E−27	−16	1.51E−10
R21*	12 515.53162	3.00E−27	2.54E−27	−15	1.49E−10
R18*	12 515.54653	3.53E−27	2.75E−27	−22	1.61E−10
R20	12 515.57663	6.16E−27	2.58E−27	−58	2.96E−10

† Perturbed transitions.
* Blended lines.

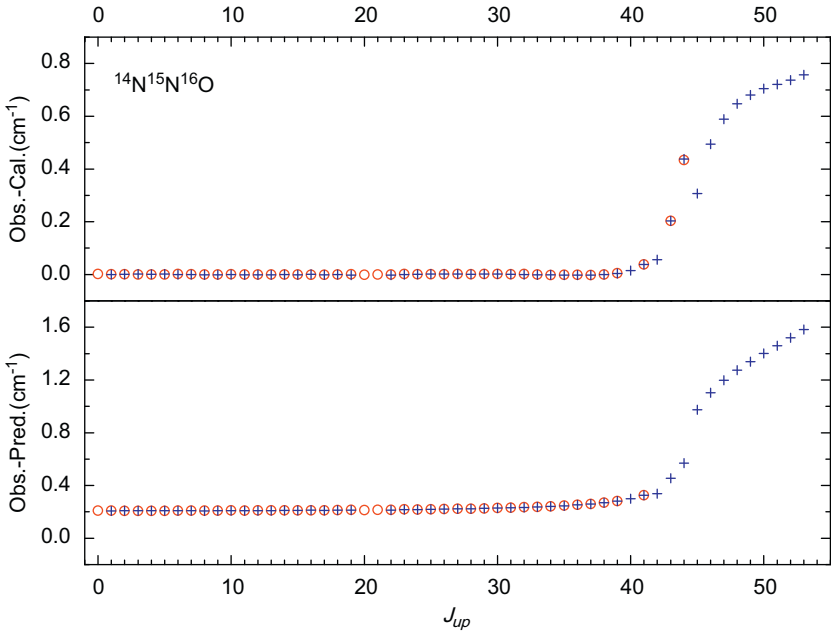

Fig. 4. Difference between the observed energy levels of the $(0\,0^0\,6)$ state of $^{14}N^{15}N^{16}O$ with the calculated values. Upper panel: deviations from the unperturbed values calculated with the spectroscopic parameters of Table 2. Lower panel: deviations from the values predicted by the effective Hamiltonian model. Circles and crosses correspond to the levels calculated from P and R transitions, respectively.

these high overtones is not as good as for the lower vibrational states. Even for those energy levels not suffering from perturbations, the deviation from the EH models exceeds 0.21, 0.33 and 0.21 cm^{-1} for 456, 546 and 556 isotopologues, respectively. According to the theoretical analysis based on the effective Hamiltonian models

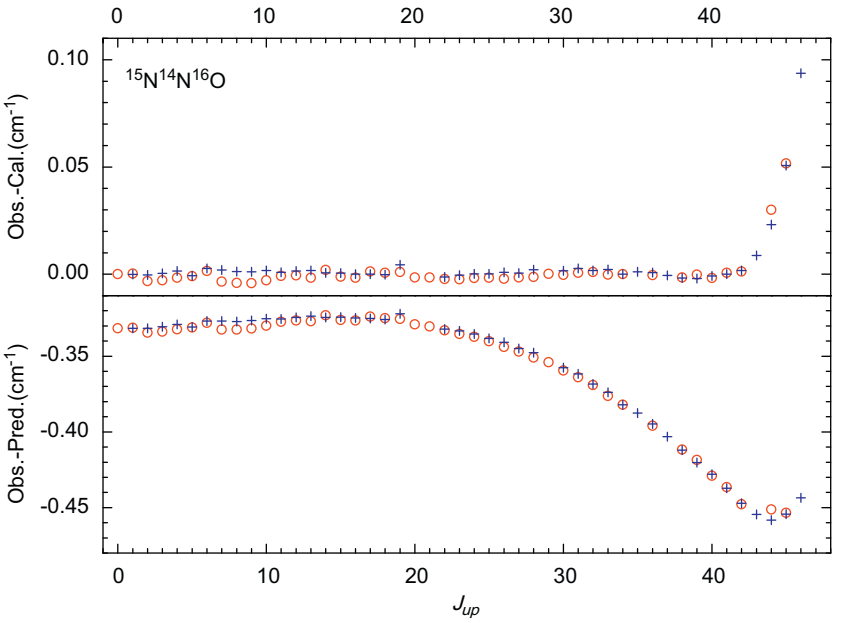

Fig. 5. Difference between the observed energy levels of the (00^06) state of $^{15}N^{14}N^{16}O$ with the calculated values. Upper panel: deviations from the unperturbed values calculated with the spectroscopic parameters of Table 2. Lower panel: deviations from the values predicted by the effective Hamiltonian model. Circles and crosses correspond to the levels calculated from P and R transitions, respectively.

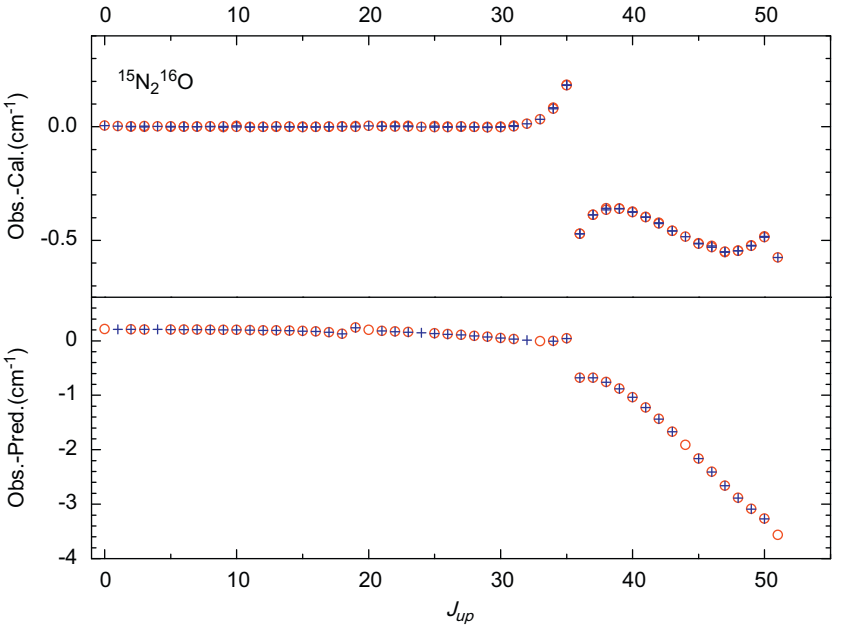

Fig. 6. Difference between the observed energy levels of the (00^06) state of $^{15}N_2^{16}O$ with the calculated values. Upper panel: deviations from the unperturbed values calculated with the spectroscopic parameters of Table 2. Lower panel: deviations from the values predicted by the effective Hamiltonian model. Circles and crosses correspond to the levels calculated from P and R transitions, respectively.

[20,21], the (00^06) states of all three isotopologues 456, 546 and 556 are perturbed by the (04^05) and (04^25) states. As a result of the anharmonic resonance interactions which involves the vibrational states (00^06) and (04^05), the overcrossing of the $6\nu_3$ and $4\nu_2+5\nu_3$ bands takes place at J equal 59, 73 and 39 for 456, 546 and 556 isotopologues, respectively. Due to the anharmonic and ℓ−type resonance interactions, local perturbations are observed for the levels near the energy level crossings of the vibrational states (00^06) and (04^25) which take place

Table 6
Summary of vibrational transition dipole moments squared and Herman–Wallis coefficients obtained for the $6v_3$ bands.

ISO	Center	Q(296 K)[a]	$\|R_0\|^2$(in 10^{-10}D^2)[b]	a_1(in 10^{-4})	a_2(in 10^{-5})
456	12 636.21	3346.66	2.615(15)	0.0[c]	3.00(48)
546	12 766.20	3444.24	2.505(17)	0.0[c]	0.85(55)
556	12 507.55	2296.16	1.567(09)	2.6(12)	−5.00(83)

[a] Values from Ref. [27].
[b] 1 debye=3.33546 × 10^{-30} cm.
[c] The values are fixed to be zero.

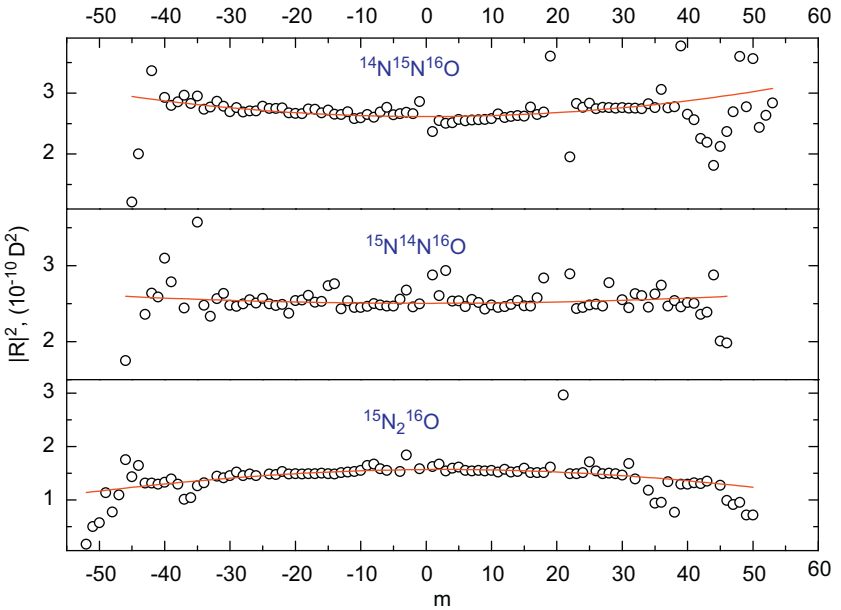

Fig. 7. Experimental (open circle) and calculated (solid line) values of the transition dipole moment squared of the $6v_3$ bands of $^{14}N^{15}N^{16}O$, $^{15}N^{14}N^{16}O$ and $^{15}N_2^{16}O$. The calculated values of $|R|^2$ are obtained using the parameters given in Table 6.

at J equal 45, 54 and 19 for 456, 546 and 556 isotopologues, respectively. As one can see from Figs. 4 to 6 the existing sets of the effective Hamiltonian parameters for all three isotopologues [20,21] do notcorrectly reproduce the observed perturbations of $6v_3$ band. No doubt that the present new experimental results will help to improve the respective sets of the effective Hamiltonian parameters.

3.3. Vibrational transition dipole moment squared and Herman–Wallis factor

The line strength $S(T_0)$ in cm^{-1}/(cm^{-2} mol) at the standard temperature T_0=296 K can be deduced using the following equation:

$$S(T_0)=\frac{1}{4\pi\varepsilon_0}\frac{8\pi^3\nu_0}{3hcQ(T_0)}|R|^2L(J,\ell)e^{-hcE''/kT_0}[1-e^{-hc\nu_0/kT_0}]. \quad (3)$$

In Eq. (3), $1/4\pi\varepsilon_0=10^{-36}$ erg cm^3 D^{-2}; h is Planck's constant; c is the vacuum speed of light; ν_0 is the transition wavenumber in cm^{-1}; $Q(T_0)$ is the total partition function at temperature T_0; $L(J,\ell)$ is the Hönl-London factor, J is the rotational quantum number of the lower state of the transition and ℓ is the quantum number of the projection of the vibrational angular momentum on the molecular axis; E'', in cm^{-1} is the energy of the lower level; k is the Boltzmann constant.

For the studied $6v_3$ cold band, the Hönl-London factor $L(J,\ell)$ is equal to $|m|$, where m is $-J$ for P branch, and J+1 for R branch. For the isolated vibrational states of a linear molecule, the rotational dependence of the transition dipole moment squared can be expressed by the well-known expansion:

$$|R|^2=|R_0|^2F(m), \quad (4)$$

where $|R|^2$ is the vibrational transition dipole moment squared, $F(m)$ is the empirical Herman–Wallis factor which can be expressed as the following:

$$F(m)=(1+a_1m+a_2m^2)^2, \quad (5)$$

where a_1 and a_2 are the Herman–Wallis coefficients. In this case, the vibrational transition dipole moment

squared and the Herman–Wallis coefficients are retrieved from the fitting of the line intensities corresponding to unperturbated transitions, and they are given in Table 6. The line intensities calculated with this set of Herman–Wallis coefficients are given in Tables 3–5 for each isotopologue, respectively. Those perturbed transitions and lines blended by water lines were marked in the tables by '†' and '∗' , respectively. In Fig. 7, the plot of the transition dipole moment squared versus rotational quantum number m is given for the $6\nu_3$ cold band of the 456, 546 and 556 isotopologues in the upper, middle and lower panels, respectively.

4. Conclusion

New experimental information about the $6\nu_3$ bands of three ^{15}N substituted nitrous oxide isotopologues and the $\nu_2+6\nu_3-\nu_2$ bands of N_2O-456 and N_2O-556 have been obtained with a CW-cavity ring-down spectrometer. Except the $\nu_2+6\nu_3-\nu_2$ band of N_2O-556, other four bands studied in this work are found to be perturbed. The comparison of the observed line positions to those predicted using effective Hamiltonian models shows that the sets of the effective Hamiltonian parameters [20,21] have to be improved. The obtained results can be applied to improve the respective effective Hamiltonian parameters. The line intensities, the vibrational transition dipole moment squared and the Herman–Wallis coefficients of the $6\nu_3$ cold band are also given.

Acknowledgments

Dr. F. Qi in NSRL is acknowledged for PIMS mass spectroscopy measurements. This work is jointly supported by NSFC-China (Grant nos. 20903085, 20873132, 10728408), by the Fok Ying Tong Education Foundation (101013), and by Chinese Ministry of Science and Technology (2006CB922001, 2007CB815203). The support of the Groupement de Recherche International SAMIA between CNRS (France), RFBR (Russia) and CAS (China) is also acknowledged.

Appendix A. Supplementary data

Supplementary data associated with this article can be found in the online version at doi:10.1016/j.jqsrt.2010.05.022.

References

[1] Weirauch G, Kachanov AA, Campargue A, Bach M, Herman M, Vander Auwera J. Refined investigation of the overtone spectrum of nitrous oxide. J Mol Spectrosc 2000;202:98–106.
[2] Andreev BA, Burenin AV, Karyakin EN, Krupnov AF, Shapin SM. Submillimeter wave spectrum and molecular constants of N_2O. J Mol Spectrosc 1976;62:125–48.
[3] Morino I, Fabian M, Takeo H, Yamada KMT. High-rotational transitions of NNO measured with the NAIR terahertz spectrometer. J Mol Spectrosc 1997;185:142–6.
[4] Drouin, Maiwald FW. Extended THz measurements of nitrous oxide, N_2O. J Mol Spectrosc 2006;236:260–2.
[5] Krell JM, Sams RL. Vibration–rotation bands of $^{14}N_2^{16}O$:1.2 micron-3.3 micron region. J Mol Spectrosc 1974;51:492–507.
[6] Amiot C. Vibration–rotation bands of $^{14}N^{15}N^{16}O$: 1.6−5.7 μm region. J Mol Spectrosc 1976;59:191–208.
[7] Guelachvili G. Absolute N_2O wavenumbers between 1118 and 1343 cm^{-1} by Fourier transform spectroscopy. Can J Phys 1982;60:1334–47.
[8] Toth RA. Frequencies of N_2O in the 1100 to 1440 cm^{-1} region. J Opt Soc Am B 1986;3:1263–81.
[9] Toth RA. Line-frequency measurements and analysis of N_2O between 900 and 4700 cm^{-1}. Appl Opt 1991;30:5289–315.
[10] Toth RA. Line positions and strengths of N_2O between 3515 and 7800 cm^{-1}. J Mol Spectrosc 1999;197:158–87.
[11] Wang L, Perevalov VI, Tashkun SA, Gao B, Hao LY, Hu SM. Fourier transform spectroscopy of N_2O weak overtone transitions in the 1−2 μm region. J Mol Spectrosc 2006;237:129–36.
[12] Herbin H, Picque N, Guelachvili G, Sorokin E, Sorokina I. N_2O weak lines observed between 3900 and 4050 cm^{-1} from long path absorption spectra. J Mol Spectrosc 2006;238:256–9.
[13] Liu AW, Kassi S, Malara P, Romanini D, Perevalov VI, Tashkun SA, et al. High sensitivity CW-cavity ring down spectroscopy of N_2O near 1.5 μm (I). J Mol Spectrosc 2007;244:33–47.
[14] Liu AW, Kassi S, Perevalov VI, Tashkun SA, Campargue A. High sensitivity CW-cavity ring down spectroscopy of N_2O near 1.5 μm (II). J Mol Spectrosc 2007;244:48–62.
[15] Liu AW, Kassi S, Perevalov VI, Hu SM, Campargue A. High sensitivity CW-cavity ring down spectroscopy of N_2O near 1.5 μm (III). J Mol Spectrosc 2009;254:20–7.
[16] Ni YH, Song KF, Perevalov VI, Tashkun SA, Liu AW, Wang L, et al. Fourier-transform spectroscopy of $^{14}N^{15}N^{16}O$ in the 3800–9000 cm^{-1} region and global modeling of its absorption spectrum. J Mol Spectrosc 2008;248:41–65.
[17] Wang CY, Liu AW, Perevalov VI, Tashkun SA, Song KF, Hu SM. High-resolution infrared spectroscopy of $^{14}N^{15}N^{16}O$ and $^{15}N^{14}N^{16}O$ in the 1200–3500 cm^{-1} region. J Mol Spectrosc 2009;257:91–104.
[18] Song KF, Liu AW, Ni HY, Hu SM. Fourier-transform spectroscopy of $^{15}N^{14}N^{16}O$ in the 3500–9000 cm^{-1} region. J Mol Spectrosc 2009;255:24–31.
[19] Gao B, Wang CY, Lu Y, Liu AW, Hu SM. High-resolution infrared spectroscopy of $^{15}N_2^{16}O$ in the 3500–9000 cm^{-1} region. J Mol Spectrosc 2010;259:20–5.
[20] Tashkun SA, Perevalov VI, Kochanov RV, Liu AW, Hu SM. Global fittings of $^{14}N^{15}N^{16}O$ and $^{15}N^{14}N^{16}O$ vibrational-d-rotational line positions using the effective Hamiltonian approach. JQSRT doi:10.1016/j.jqsrt.2010.01.010.
[21] Lyulin OM, Jacquemart D, Lacome N, Tashkun SA, Perevalov VI. Line parameters of $^{15}N_2^{16}O$ from Fourier transform measurements in the 5800–7600 cm^{-1} region and global fitting of line positions from 1000 to 7600 cm^{-1}. JQSRT 2010;111:345–56.
[22] Rothman LS, Gordon IE, Barbe A, Chris Benner D, Bernath PF, Birk M, et al. The HITRAN 2008 molecular spectroscopic database. JQSRT 2009;110:533–72.
[23] Gao B, Liu AW, Wu RX, Ning W, Hu SM. C_2H_2 overtones near 12300 cm^{-1} revisited with a very sensitive cavity ring-down spectrometer. Chin J Chem Phys 2009;22:663–7.
[24] Gao B, Jiang W, Liu AW, Lu Y, Cheng CF, Cheng GS, et al. Ultra sensitive near-infrared cavity ring down spectrometer for precise line profile measurement. Rev Sci Instrum 2010;81:043105.
[25] Halmer D, Basum GV, Hering P, Müartz M. Fast exponential fitting algorithm for real-time instrumental use. Rev Sci Instrum 2004;75:2187–91.
[26] Toth RA. Available from: 〈http://mark4sun.jpl.nasa.gov/n2o-html〉.
[27] Toth RA. Line strengthes (900–3600 cm^{-1}), self-broadened linewidths, and frequency shifts (1800–2360 cm^{-1}) of N_2O. Appl Opt 1993;32:7326–65.